LASER & PHOTONICS REVIEWS

Laser Photonics Rev. **10,** No. 4, 595–602 (2016) / **DOI** 10.1002/lpor.201500179

ORIGINAL PAPER

Abstract Light manipulation is paramountly important to the fabrication of high-performance optoelectronic devices such as solar cells and photodetectors. In this study, a high-performance near-infrared light nanophotodetector (NIRPD) was fabricated based on a germanium nanoneedles array (GeNNs array) with strong light confining capability, and single-layer graphene (SLG) modified with heavily doped indium tin oxide nanoparticles (ITONPs), which were capable of inducing localized surface plasmon resonance (LSPR) under NIR irradiation. An optoelectronic study shows that after modification with ITONPs the device performance including photocurrent, responsivity and detectivity was considerably improved. In addition, the ITONPs@SLG/GeNNs array NIRPD was able to monitor fast-switching optical signals, the frequency was as high as 1 MHz, with very fast response rates. Theoretical simulations based on finite-element method (FEM) revealed that the observed high performance was not only due to the strong light-confining capability of the GeNNs array, but also due to the plasmonic ITONPs-induced hot electron injection. The above results suggest that the present NIRPD will have great potential in future optoelectronic devices application.

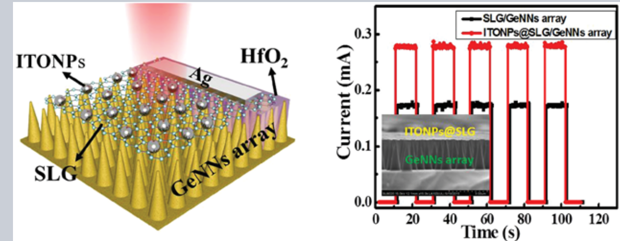

A localized surface plasmon resonance and light confinement-enhanced near-infrared light photodetector

Rui Lu, Cai-Wang Ge, Yi-Feng Zou, Kun Zheng, Dan-Dan Wang, Teng-Fei Zhang, and Lin-Bao Luo*

1. Introduction

Localized surface plasmon resonance (LSPR) is known to be the collective oscillation of electrons gas in nanoscale solids when stimulated by incident light. Plasmonic metal nanostructures (e.g. Au, Ag, Pt and Al) with high sensitivity of optical response to the surrounding environment have proved to be promising platforms for various biosensing applications [1, 2]: such as surface enhanced Raman spectroscopy [3], theranostics [4], biomolecular interaction examination [5], and gas sensing [6–8]. In addition, plasmonic nanomaterial has also been regarded as one of the most efficient light-trapping platforms to boost the performance of light-harvesting optoelectronics in that it is capable of coupling and trapping freely propagating plane waves into an adjacent semiconductor. By this token, plasmonic metal nanostructures have been widely applied in a number of fields [9, 10], such as inorganic material solar cells [11–13], organic photovoltaic devices [14, 15], nanoantennas [16–18], electrochromic devices [19], light-emitting diodes (LEDs) [20, 21], photocalalysts [22, 23], water splitters [24, 25], and photodetectors [26–30].

The excitation of LSPR fundamentally relies on the interaction between free charge carries and incident light. Although LSPR has been widely observed in a number of metals with high electron density, some nonmetal semiconductor nanostructures are able to exhibit obvious LSPR as well [31, 32], which is attributed to the availability of a high density of free charge carrier (electrons or holes) as a result of controlled doping [33]. For example, nonstoichiometric copper chalcogenides (e.g. $Cu_{2-x}S$, $Cu_{2-x}Se$ and $Cu_{2-x}Te$) were found to exhibit a tunable and reversible LSPR band in the range of 900–1800 nm by controlled oxidation of monovalent copper [34]. Furthermore, impurity atom-doped metal oxides such as $Sn{:}In_3O_2$, Al:ZnO, Ga:ZnO and $Nb{:}TiO_2$ have also displayed tunable LSPR. More recently, strong LSPR has been observed in other nonstoichiometric high-valence metal oxides (XO_{3-x}: X = Re, Mo and W) due to high carrier density [35, 36]. In spite of these tremendous efforts, most of the work mentioned above has dealt with the synthesis and optics of nonmetal plasmonic nanostructures, and there are few reports about the utilization of nonmetal plasmonic materials for optoelectronic devices application. Herein, a high-performance NIR light photodetector was fabricated by introducing plasmonic tin-doped indium oxide nanoparticles (ITONPs) into a nanoheterojunction. Unlike conventional noble-metal nanocrystals normally with tunable LSPR band in the visible and UV region, the present heavily doped ITONPs exhibited typical LSPR in the NIR region, which was completely compatible with the detection of NIR irradiation. Both theoretical simulation and device analysis revealed that the plasmonic ITONPs were capable of inducing near-field enhancement and injecting hot electrons into the SLG, leading to an obvious increase in photocurrent, responsivity and detectivity.

School of Electronic Science and Applied Physics, Hefei University of Technology, Hefei, Anhui 230009, P. R. China
*Corresponding author: e-mail: luolb@hfut.edu.cn

© 2016 by WILEY-VCH Verlag GmbH & Co. KGaA, Weinheim

2. Experimental section

Preparation and characterization of ITONPs, GeNNs array and SLG film: The heavily doped ITONPs were synthesized by a reflux method in oleylamine, in which the doping level of Sn was controlled by tuning the In/Sn precursor ratios (detailed information about the synthetic process was described by Kaneharra et al. [37]). The vertical GeNNs array was prepared through a silver-catalyzed HF etching method. In brief, n-type (100) single-crystalline Ge wafers (size: 4 × 8 mm^2) were treated in acetone, ethanol and deionized water for several times to remove contamination or organic grease. Highly ordered hexagonal-packed monolayer polystyrene (PS) spheres (~900 nm) were allowed to self-assemble on the clean Ge substrate by a slow-pulling strategy. The close-packed single-layer assembly was then treated by reactive ion etching (RIE) to form a nonclose-packed PS. Afterwards, an electron beam evaporator was used to coat a 20-nm thick silver film on the Ge wafer, followed by dipping into the mixed solution composed of deionized water, HF, and H_2O_2 (the concentrations of HF and H_2O_2 were 4.8 and 0.2 M, respectively). After etching, the wafers were taken out and then dipped in acetone to dispel the polymer spheres [38, 39]. The remaining Ag film was finally removed by immersing in a solution composed of deionized water, $NH_3.H_2O$, and H_2O_2. Then, the sample was rinsed with deionized water, and dried at ambient condition. The SLG films were grown by a conventional Cu-catalyzed chemical vapor deposition (CVD) method, which was carried out at 1000°C using a mixed gas of methane (40 SCCM) and hydrogen gas (20 SCCM) as the reaction source. The as-synthesized thin film were then spin-coated with 5 wt% polymethylmethacrylate (PMMA) and then immersed in an etch solution ($CuSO_4$:HCl:H_2O = 10 g:50 mL:50 mL) to remove the catalytic Cu foil.

Device construction and characterization: To assemble the ITONPs@SLG/GeNNs array Schottky junction photodetector, a HfO_2 film was first deposited on one side of the GeNNs array using magnetron sputtering for the sake of insulation. Then, the above PMMA-supported SLG was transferred onto the top of the GeNNs array and dried on a hotplate at 100°C for 10 min, followed by removal of the PMMA by acetone. A drop of silver paste was then placed at the SLG where the HfO_2 film was deposited. Finally, the ITONPs were modified onto the SLG by spin coating the ITONPs suspension. The electrical property assessment of the NIRPD device was performed on a semiconductor *I–V* characterization system (4200-CSC, Keithley Co., Ltd.). The optoelectronic properties of the NIRPD were studied by using a 1550-nm laser (Thorlabs-PPL1055T) as a light source. Furthermore, to determine the response rate of the NIRPD, a home-built system composed of an oscilloscope (Tektronix, TDS2012B), and a 1550-nm laser driven by a high-frequency generator was used.

Theoretical simulation: The modeling was performed by the finite-element method (FEM). During simulation, the incident light is set to be an x-polarized plane wave propagating along the $-z$-axis. Boundary conditions of perfect magnetic conductors (PMCs) were used for $y = 0$ and $y = L/2$ planes, and perfect electric conductors (PECs) conditions were used for the other two planes, $x = 0$ and $x = L/2$. Perfect matched layers (PMLs) were used at the top and bottom of the model and ended with the scattering boundaries. The graphene layer was considered as an infinitely thin conducting layer, and treated as the transition boundary condition. The optical data of Ge were from the Sopra S. A. company database and those of ITO were from the E. F. Schubert's Handbook of Optics. The optical date of graphene was described by the $\sigma 0$ model [40].

3. Results and discussion

The proof-of-concept NIRPD is composed of a free-standing GeNNs array [Fig. 1a], and a SLG film decorated with heavily doped ITONPs, which were fabricated by a reflux method in oleylamine [37]. The doping level of the Sn atoms can be controlled by changing the In/Sn precursor ratio. Figure S1 shows the XRD patterns of ITONPs with doping levels from 5–30%. It is revealed that all peaks can be readily ascribed to the phase of In_2O_3 NPs, and no obvious impurity peaks due to either SnO or SnO_2 are observed (supporting information). This result suggests that the Sn atoms have replaced the In atoms in the crystal lattice to provide sufficient donors in the nanostructures, leading to high carrier density to support LSPR. Figure 1b shows the TEM image of ITONPs with 10% Sn doping. The diameters of the ITONPs are in the range of 15–25 nm, with an average value of 21 nm. Further HRTEM analysis [inset of Fig. 1b] depicts that the as-prepared ITONP is single crystalline, and the *d*-spacing of the adjacent lattice of ITONPs is ~0.21 nm, corresponding to the (422) plane of ITO (JCPDF No. 06–0416). In fact, the Sn doping is also verified by energy-dispersive spectroscopy (EDS) and X-ray photoelectron spectroscopy (XPS) analysis (Figs. S2 and S3). Furthermore, the single layer of graphene is consistent with the Raman analysis shown in Fig. 1c, from which an intensity ratio of I_{2D}:I_G ≈2.49 was obtained. The negligible *D*-band at ~1320 cm^{-1} indicates the high quality of the SLG. The highly ordered n-GeNNs array with identical period and dimension was fabricated by a metal-assisted chemical etching approach, prior to which a silver film with hexagonal nanoholes was defined by a polystyrene (PS) nanosphere lithography technique, followed by reactive ion etching (RIE) treatment [41]. Since the length of the GeNNs is primarily determined by the etch duration, GeNNs with different lengths can be easily obtained by tuning the etch time.

Figure 2a shows a representative SEM image of an NIRPD that consists of ITONPs-modified SLG and free-standing GeNNs array (Structure I) with a height of ~3 μm. To minimize the surface-state density, the GeNNs array was immersed in an aqueous HF to remove native oxide, followed by chemical passivation through a hot $(NH_4)_2S$ solution [22% (v/v)] [42]. Figure 2b plots the absorption curves

© 2016 by WILEY-VCH Verlag GmbH & Co. KGaA, Weinheim

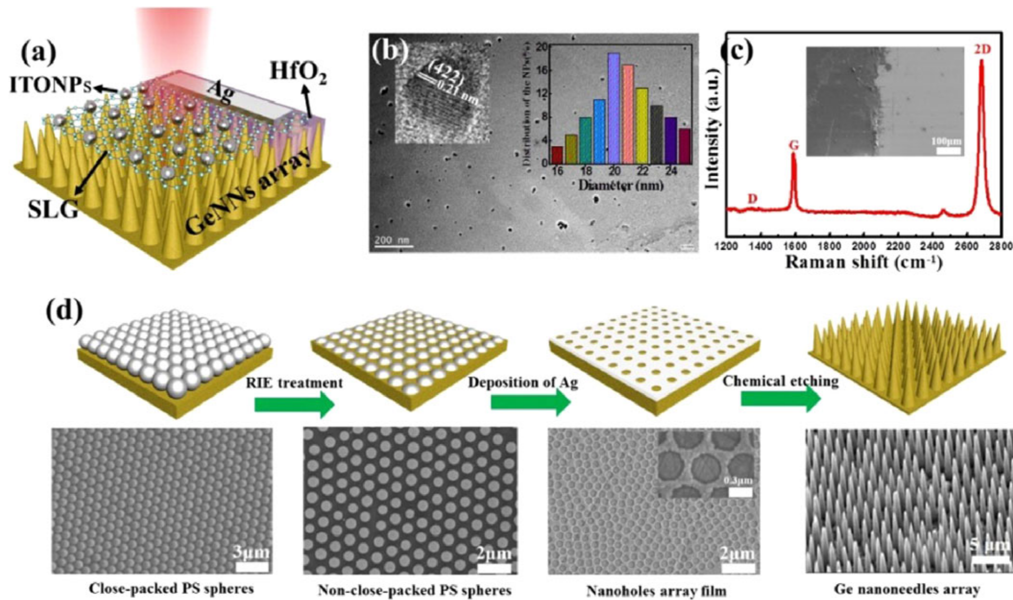

Figure 1 (a) The schematic illustration of the ITONPs@SLG/GeNNs array NIRPD. (b) TEM image of ITONPs, the above left and right insets are the HRTEM image and size distribution of the ITONPs, respectively. (c) Raman analysis of the SLG, the inset is SEM image of the SLG on Ge wafer. (d) Schematic illustration of the procedures for fabricating GeNNs, the SEM images show the corresponding morphologies.

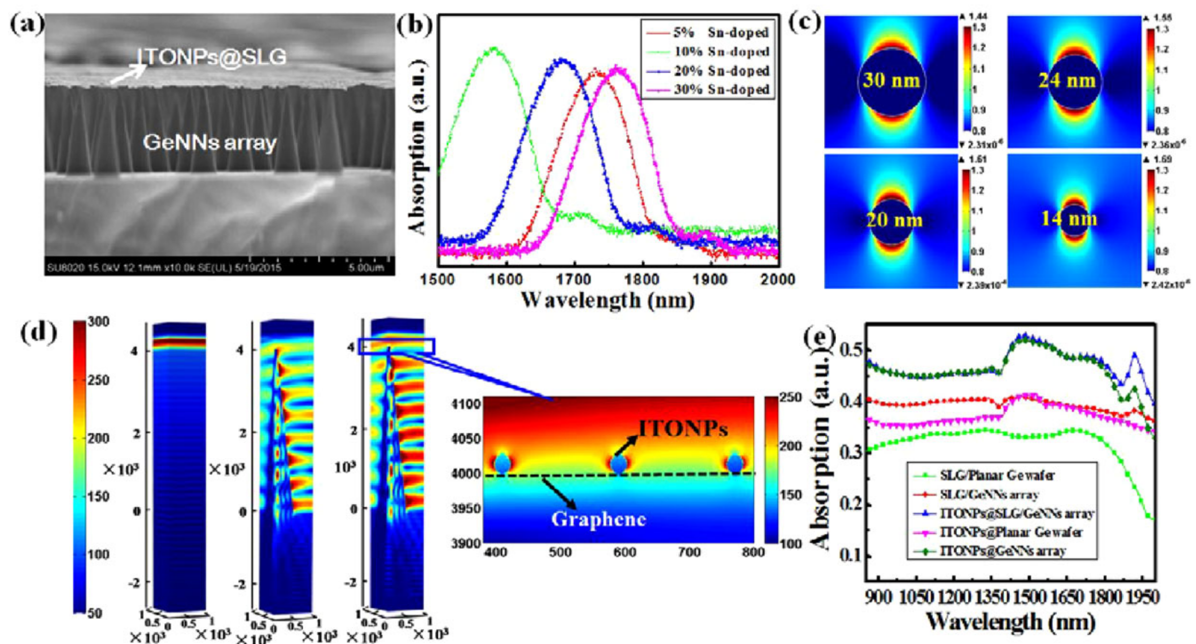

Figure 2 (a) SEM image of Structure I NIRPD. (b) The absorption of ITONPs with different doping levels. (c) The electric-field intensity distribution of ITONPs (Sn10%) with different diameters. (d) Electric-field energy-density distribution of Ge, Structure I, and Structure II under 1550-nm illumination. (e) The experimental absorption spectra collected from Structure I, II, and III, ITONPs@planar Ge wafer and ITONPs@GeNNs array.

of variously doped ITONPs, in which strong absorption peaks due to LSPR are found to depend on the doping level of the NPs. Remarkably, with the increase of Sn doping level from 5% to 10%, 20% and 30%, the wavelength of the LSPR peak was observed to firstly blueshift from 1730 to 1580 nm, and then redshift 1680 to 1760 nm. Such a doping level-dependent LSPR peak is due to the following reason: In the lattice structure of a ITO nanoparticle, a Sn atom can replace an In atom, giving rise to a free electron. In the low-doping range (1–10%), higher %Sn usually leads

© 2016 by WILEY-VCH Verlag GmbH & Co. KGaA, Weinheim

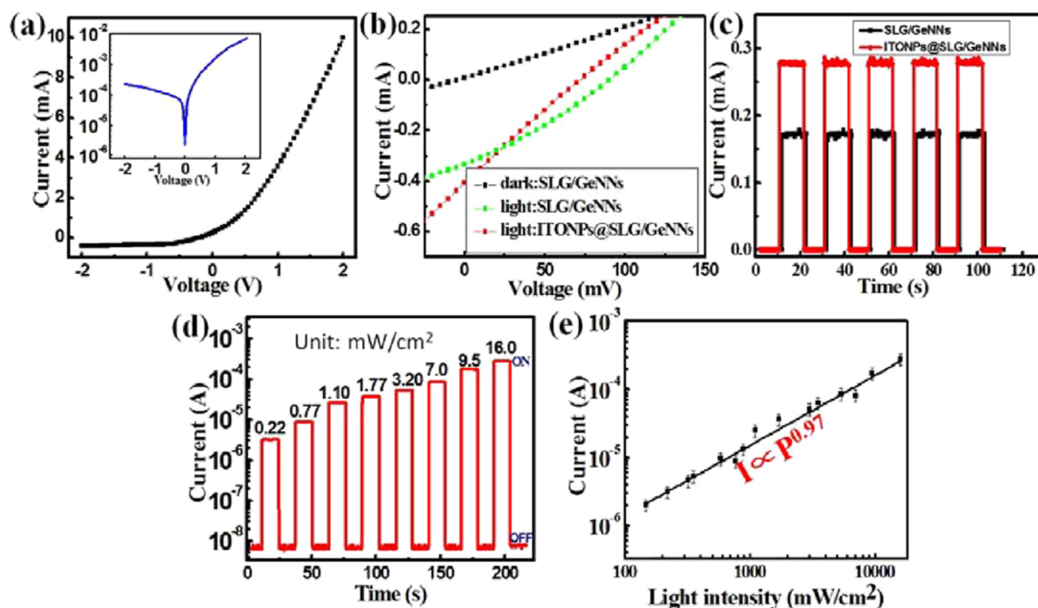

Figure 3 (a) Typical rectification characteristics of the NIRPD in dark. (b) Photovoltaic characteristics of the Structure I and II Schottky junctions. (c) Photoresponse of two representative devices with and without ITONPs modification under 1550-nm light illumination at $V_{\text{bias}} = 0$ V. (d) Photoresponse of the Structure I array NIRPD under various light intensities. (e) The fitting of the relationship between the photocurrent and light intensity.

to higher free electron density. However, further increase in Sn doping level can cause electron trapping around the Sn atoms, leading to a decrease of the electron density and therefore a longer LSPR wavelength [43]. In fact, the LSPR effect is also confirmed by the simulated near-field intensity distribution of ITONPs. As shown in Fig. 2c, all the ITONPs with diameters in the range of 14–30 nm can induce obvious enhancement in the dipolar electric energy under irradiation of 1550-nm light. Since the ITONPs were fabricated by a reflux method, and they were further decorated on the SLG by a simple spin-coating approach. Such synthesis and decoration methods lead to randomly distributed ITONPs array. Therefore, it is nearly impossible to induce collective lattice resonance (Fano-like resonance) in this case [44]. To disclose the effect of the plasmonic ITONPs on the optical property of the SLG/GeNNs (Structure II) Schottky junction, the electrical field-density distributions of both Structure I and II with and without ITONPs were compared by theoretical simulation based on FEM [Fig. 2d]. It is seen that a strong electric field (hot spots) can be observed at both central and superficial parts of the GeNNs when illuminated by NIR light. This finding is different from the electrical-field distribution of SLG/planar Ge (Structure III) where only plane-wave profiles were observed, suggesting the strong light-confinement capability of the GeNNs array. Remarkably, such a light-trapping effect can be further enhanced by the introduction of the plasmonic ITONPs on the SLG surface. In this case, the Structure I heterojunction is essentially an SPP-based light-coupling regime in which the plasmonic ITONPs can function as subwavelength scattering elements to couple and trap freely incident NIR light into the GeNNs array [10]. Figure 2e plots the absorption spectra of the three nanostructures in the NIR range. In comparison with both Structure II and III, Structure I exhibited the strongest light absorption due to the combination of both LSPR effect and light trapping. It is worth noting that during this study, two other structures ("a graphene-coated Ge layer with a NP decoration": Structure A; and "a GeNNs array decorated with ITO particles without a graphene flake": Structure B) are also considered. However, further experimental analysis finds that the performance of the device based on Structure A is rather poor. Understandably, the poor device performance is probably related to the weak light absorption of the planar Ge wafer relative to that of GeNNs array (Fig. S4). On the other hand, even though Structure B may exhibit even stronger light absorption than the GeNNs array, due to the absence of graphene, however, no built-in electric field was formed in the device. As a result, the photogenerated electron–hole pairs cannot be efficiently separated, leading to no photocurrent in the device. In light of the above analysis, the ITONPs@SLG/GeNNs array (Structure I) is the best choice from the perspectives of both optical property and carrier collection.

An electrical study reveals that the as-fabricated device with plasmonic ITONPs displays obvious rectifying behavior because of the Schottky barrier between SLG and the n-GeNNs array [Fig. 3a]. From the I–V curves, the rectification ratio is determined to be $\sim 10^2$. In addition, the turn-on voltage is derived to be 0.3 V, which is relatively smaller than that of SLG/GaAs nanocones [39], and SLG/ZnO nanorods [27]. By using the thermionic emission-based diode equation (Supporting information) [45], the barrier height of the Schottky junction is calculated to be 0.47 V,

© 2016 by WILEY-VCH Verlag GmbH & Co. KGaA, Weinheim

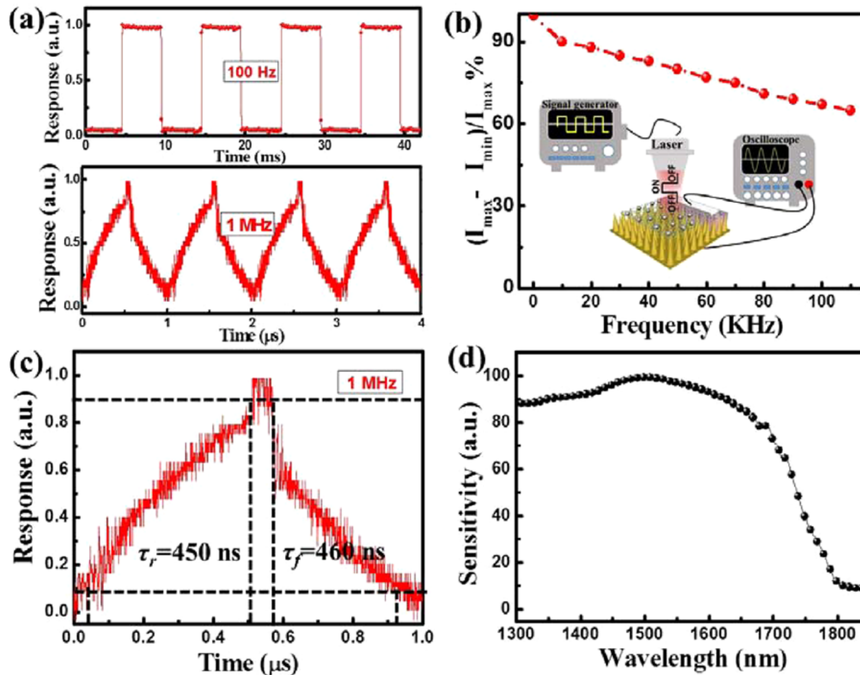

Figure 4 (a) The relative balance $(I_{max} - I_{min})/I_{max}$ versus switching frequency, the inset shows the schematical illustration of the experimental setup for studying the time response of the NIRPD. (b) Photoresponse of the device to pulsed NIR irradiation at a frequency of 100 Hz and 1 MHz. (c) One normalized cycle measured at 1 MHz for estimating both rise time (τ_r) and fall time (τ_f). (d) Spectral response of a NIRPD.

comparable to that of Structure II (0.45 V), signifying that the ITONPs modification can hardly alter the nature of the Schottky junction. Figure 3b compares the photovoltaic characteristics of two devices with and without ITONPs when exposed to 1550-nm illumination. The open-circuit voltages (V_{oc}) at zero bias voltage are estimated to be 0.055 and 0.39 V for Structures II and I, respectively. As discussed later, the relatively large photovoltage is related to the LSPR effect of ITONPs. Although the power conversion efficiency (PCE) is very low (~0.23%), the plasmonic nanoheterojunction can act as a self-driven device that is capable of sensing NIR illumination without power supply. Figure 3c depicts the photosensitivity of devices with and without decoration of plasmonic nanocrystals. It is seen that both devices can be reproducibly switched between low- and high-resistance states when the NIR irradiation was turned on and off repeatedly. The photocurrent for Structure I is 0.26 mA, which is much larger than those for both Structure II (0.18 mA) and Structure III (0.07 mA). Moreover, the on/off ratios are determined to be 3×10^4, and 5×10^4 for Structure II and I, respectively. Further device analysis reveals that the photocurrent (I_p) of the Structure I is completely dependent on the intensity of NIR light [Fig. 3d]. In fact, this relationship can be represented by a power law: $I_p = AP^\theta$, where A is a constant for a specific wavelength, P the power of NIR irradiation, and θ the exponent ($0.5 < \theta < 1$) that determines the photoresponse of photocurrent to NIR illumination, respectively. By carefully fitting the above formula to the photocurrent–intensity curve, the θ is calculated to be ~0.97 [Fig. 3e]. Such a near-integer θ verifies the good quality of the present NIRPD.

Next, in order to quantitatively delineate the device performance of NIRPD, two important device metrics, responsivity (R) and detectivity (D^*), were estimated by using the following relations [46]:

$$R\left(AW^{-1}\right) = \frac{I_p - I_d}{P_{opt}} = \eta\left(\frac{q\gamma}{hc}\right)G \quad (1)$$

$$D^* = \sqrt{\frac{A}{2qI_d}}R, \quad (2)$$

where I_p is the current under light illumination, I_d is current in dark, P_{opt} is the power of the incident NIR light, η is the quantum efficiency (assuming $\eta = 1$ for simplification), h is the Planck constant (6.626×10^{-34} J s), c is the light speed (2.997×10^8 m/s), λ *is* the illumination wavelength (1550 nm), A is the effective area of the NIRPD, and q is the unit of elementary charge (1.6×10^{-19} C). In this case, the light intensity is 5 mW/cm^2, and the area of the Structure I NIRPD is 0.3025 cm^2. Therefore, the R and D^* are estimated to be 185 mA W^{-1} and 2.28×10^{13} cm Hz$^{1/2}$ W^{-1}, respectively. Besides the high responsivity and detectivity, the present plasmonic device is also characterized by a fast response rate. Figure 4a plots the optoelectronic property of the NIRPD under fast-switching irradiation. It is seen that the device can be reproducibly switched between "on" and "off" states even though the frequency of the NIR irradiation exceeds 1 MHz. Further investigation showed that the relative balance ($I_{max} - I_{min}/I_{max}$) of the NIRPD only decreases by less than 30% when the frequency is increased to 110 kHz. To estimate the response rate, one normalized cycle of response to 1 MHz illumination was provided in Fig. 4c, from which the rise time (τ_r, time needed for the photocurrent to increase from 10 to 90%)

© 2016 by WILEY-VCH Verlag GmbH & Co. KGaA, Weinheim

Table 1 Summary of the device performance of the present NIRPD and other devices with similar structures

Materials	Responsivity	τ_r/τ_f	I_{on}/I_{off}	Detectivity (Jones)	Ref
Structure I	185 mA/W	450/460 ns	5×10^4	2.28×10^{13}	This work
Structure II	92 mA/W	22/50 μs	$\sim 3 \times 10^4$	3.57×10^{11}	This work
SLG/Ge wafer	51.8 mA/W	23/108 μs	2×10^4	1.38×10^{10}	[51]
SLG/GaAs nanocone array	1.73 mA/W	72/122 μs	10^4	1.83×10^{11}	[39]
Ge nanowire	—	0.2/1 s	$\sim 10^2$	—	[52]

and fall time (τ_f, time needed for the photocurrent to decrease from 90 to 10%) were derived to be 450 and 460 ns, respectively. Such a response rate is much faster than that of Structure II (Fig. S5), and other devices with similar device geometries (Table 1). Two factors are considered significant to the fast response rate: (1) The high quality of the GeNNs. The GeNNs array obtained via the chemical etch method is single crystal with few trapping centers as a result of surface passivation. This feature is beneficial for the fast achievement of steady states for photocurrent. (2) The decoration of plasmonic ITONPs. Although the underlying reason for this improvement is still unknown, a similar phenomenon has been observed in other noble-metal plasmonic nanoparticle-based devices [47, 48]. It is also revealed that the present device exhibits excellent spectral selectivity in the wavelength range from 1300–1850 nm. As shown in Fig. 4d, the NIRPD shows the highest sensitivity in the range from 1400–1600 nm, but it is nearly blind to NIR illumination with wavelengths larger than 1800 nm. Table 1 lists the device performance of the present NIRPD and other photodetectors with similar device configurations. Apparently, several key device parameters including responsivity, response rate, on/off ratio, and detectitivity are higher than not only those composed of SLG/Ge wafer and Ge NWs, but also than that based on SLG/GaAs nanocones array. Without question, the good device performance as well as the spectral response renders the present NIRPD highly promising for future photodetection applications, especially in telecommunications.

The high sensitivity of the present NIRPD is related to the operational mechanism. Figure S6 illustrates the energy-band diagram of the Structure I array. Owing to the difference in work functions between the n-type Ge and graphene, the electrons in Ge move to SLG and the energy level near the Ge bends upward to form a built-in electric field (depletion region) near the SLG-Ge interface. Under 1550-nm light illumination, the built-in electric field can separate the photogenerated excitons (electron-holes pairs), causing the formation of photocurrent in external circuit. Remarkably, such a photocurrent-generation process was greatly facilitated when plasmonic ITONPs were decorated on the SLG surface. In this case, the energetic hot electrons within ITONPs as a consequence of LSPR can couple the resonant energy, and then transfer to SLG. The injected electrons at the depletion region were then separated by the electric field [49]. It should be pointed out that such an injection of hot electrons is highly spontaneous under NIR illumination due to the high energy of hot electrons (1–4 eV) [50], and low Schottky barrier between the heavily doped ITONPs and SLG.

4. Conclusion and outlook

In summary, a high-performance near-infrared nanophotodetector (NIRPD) has been successfully fabricated by coating germanium nanoneedle arrays (GeNNs) with non-metal plasmonic indium tin oxide nanoparticles (ITONPs)-decorated single-layer graphene (SLG). Device analysis finds that the NIRPD exhibits high sensitivity to 1500-nm illumination under zero bias with a high response speed (response/recovery time of 450/460 ns), excellent spectral selectivity and good reproducibility in a wide range of switching frequency (100 Hz–1 MHz). In addition, the on/off ratio, responsivity and detectivity of the device were estimated to be 5×10^4, 185 mA/W and 2.28×10^{13} cm Hz$^{1/2}$ W^{-1}, respectively. Theoretical simulation of the ITONPs@SLG/GeNNs array based on a finite-element method (FEM) reveals that the excellent device performance is mainly attributed to the light confinement effect of GeNNs array, and plasmonic ITONPs-induced electron injection. The totality of this study suggests that the present plasmonic NIRPD will have promising potential for next-generation optoelectronic devices and systems.

With the rapid development of synthetic technology, plasmonic materials-based non-noble metal nanostructures have enormously emerged and they display great potential due to their low cost and tunable localized surface plasmon resonance (LSPR) frequency [38]. However, it is undeniable that the study of combination of these kinds of materials for optoelectronic devices is still in its infancy and needs extensive investigation. Among the various non-noble-metal plasmonic materials, the heavily doped semiconductor nanostructure, in particular heavily doped silicon, will be the most promising building block for integrating high-performance plasmonic optoelectronic devices due to its ready compatibility with modern semiconductor technology.

© 2016 by WILEY-VCH Verlag GmbH & Co. KGaA, Weinheim

Supporting Information

Additional supporting information may be found in the online version of this article at the publisher's website.

Acknowledgements. This work was supported by the Natural Science Foundation of China (NSFC, No. 61575059, 21101051), and the Fundamental Research Funds for the Central Universities (2012HGCX0003, 2013HGCH0012, 2014HGCH0005).

Received: 30 July 2015, **Revised:** 9 April 2016,
Accepted: 13 April 2016

Published online: 3 May 2016

Key words: Nonmetal plasmonic nanoparticles, heavily doped semiconductor nanocrystals, near-infrared light photodetector, responsivity, nanoheterojunction.

References

[1] P. Zijlstra and M. Orrit, Rep. Prog. Phys. **74**, 106401 (2011).
[2] K. M. Mayer and J. H. Hafner, Chem. Rev. **111**, 3828–3857 (2011).
[3] L. B. Luo, L. M. Chen, M. L. Zhang, Z. B. He, W. F. Zhang, G. D. Yuan, W. J. Zhang, and S. T. Lee, J. Phys. Chem. C. **113**, 9191–9196 (2009).
[4] E. C. Dreaden, A. M. Alkilany, X. H. Huang, C. J. Murphy, and M. A. El-Sayed, Chem. Soc. Rev. **41**, 2740–2779 (2012).
[5] S. C. B. Gopinath and P. K. R. Kumar, Analyst **139**, 2678–2682 (2014).
[6] A. Tittl, H. Giessen, and N. Liu, Nanophotonics **3**, 157–180 (2014).
[7] N. Liu, M. L. Tang, M. Hentschel, H. Giessen, and A. P. Alivisatos, Nature Mater. **10**, 631–636 (2011).
[8] S. B. Wang, Y. F. Huang, S. Chattopadhyay, S. J. Chang, R. S. Chen, C. W. Chong, M. S. Hu, L. C. Chen, and K. H. Chen, NPG Asia Mater. **5**, (2013).
[9] V. E. Ferry, J. N. Munday, and H. A. Atwater, Adv. Mater. **22**, 4794–4808 (2010).
[10] R. F. Oulton, V. J. Sorger, D. A. Genov, D. F. P. Pile, and X. Zhang, Nature Photon. **2**, 496–500 (2008).
[11] H. A. Atwater and A. Polman, Nature Mater. **9**, 205–213 (2010).
[12] L. B. Luo, C. Xie, X. H. Wang, Y. Q. Yu, C. Y. Wu, H. Hu, K. Y. Zhou, X. W. Zhang, and J. S. Jie, Nano Energy. **9**, 112–120 (2014).
[13] S. Pillai, K. R. Catchpole, T. Trupke, and M. A. Green, J. Appl. Phys. **101**, 093105 (2007).
[14] X. H. Li, W. C. H. Choy, L. J. Huo, F. X. Xie, W. E. I. Sha, B. F. Ding, X. Guo, Y. F. Li, J. H. Hou, J. B. You, and Y. Yang, Adv. Mater. **24**, 3046–3052 (2012).
[15] X. H. Li, W. C. H. Choy, H. F. Lu, W. E. I. Sha, and A. H. P. Ho, Adv. Funct. Mater. **23**, 2728–2735 (2013).
[16] X. J. Ni, N. K. Emani, A. V. Kildishev, A. Boltasseva, and V. M. Shalaev, Science, **335**, 427 (2012).
[17] Z. T. Liu, A. Boltasseva, R. H. Pedersen, R. Bakker, A. V. Kildishev, V. P. Drachev, and V. M. Shalaev, Metamater. **2**, 45–51 (2008).
[18] T. Kang, W. Choi, I. Yoon, H. Lee, M. K. Seo, Q. H. Park, and B. Kim, Nano Lett. **12**, 2331–2236 (2012).
[19] A. Tsuboi, K. Nakamura, and N. Kobayashi, Adv. Mater. **25**, 3197–3201 (2013).
[20] M. K. Kwon, J. Y. Kim, B. H. Kim, I. K. Park, C. Y. Cho, C. C. Byeon, and S. J. Park, Adv. Mater. **20**, 1253–1257 (2008).
[21] K. Okamoto, I. Niki, A. Shvartser, Y. Narukawa, T. Mukai, and A. Scherer, Nature Mater. **3**, 601–605 (2004).
[22] W. B. Hou and S. B. Cronin, Adv. Funct. Mater. **23**, 1612–1619 (2013).
[23] E. Kowalska, O. O. P. Mahaney, R. Abe, and B. Ohtani, Phys. Chem. Chem. Phys. **12**, 2344–2355 (2010).
[24] X. Zhang, Y. Liu, S. T. Lee, S. H. Yang, and Z. H. Kang, Energy Environ. Sci. **7**, 1409–1419 (2014).
[25] D. B. Ingram and S. Linic, J. Am. Chem. Soc. **133**, 5202–5205 (2011).
[26] B. Y. Zheng, Y. M. Wang, P. Nordlander, and N. J. Halas, Adv. Mater. **26**, 6318–6323 (2014).
[27] Z. Y. Fang, Z. Liu, Y. M. P. M. Ajayan, P. Nordlander, and N. J. Halas, Nano Lett. **12**, 3808–3813 (2012).
[28] P. Berini, Laser Photon. Rev. **8**, 197–220 (2014).
[29] A. Pescaglini, A. Martin, D. Cammi, G. Juska, C. Ronning, E. Pelucchi, and D. Iacopino, Nano Lett. **14**, 6202–6209 (2014).
[30] L. B. Luo, L. H. Zeng, C. Xie, Y. Q. Yu, F. X. Liang, C. Y. Wu, L. Wang, and J. G. Hu, Sci. Rep. **4**, 3914 (2014).
[31] Y. X. Zhao, H. C. Pan, Y. B. Lou, X. F. Qiu, J. J. Zhu, and C. Burda, J. Am. Chem. Soc. **131**, 4253–4261 (2009).
[32] Q. Q. Huang, S. Hu, J. Zhuang, and X. Wang, Chem. Eur. J. **18**, 15283–15287 (2012).
[33] J. M. Luther, P. K. Jain, T. Ewers, and A. P. Alivisatos, Nature Mater. **10**, 361–366 (2011).
[34] X. Liu and M. T. Swihart, Chem. Soc. Rev. **43**, 3908–3920 (2014).
[35] K. Manthiram and A. P. Alivisatos, J. Am. Chem. Soc. **134**, 3995–3998 (2012).
[36] K. Biswas and C. N. R. Rao, J. Phys. Chem. B. **110**, 842–845 (2006).
[37] M. Kanehara, H. Koike, T. Yoshinaga, and T. Teranishi, J. Am. Chem. Soc. **131**, 17736–17727 (2009).
[38] L. B. Luo, Y. F. Zou, C. W. Ge, K. Zheng, D. D. Wang, R. Lu, T. F. Zhang, Y. Q. Yu, and Z. Y. Guo, Adv. Opt. Mater. DOI: 10.1002/adom.201500701 (2016).
[39] L. B. Luo, J. J. Chen, M. Z. Wang, H. Hu, C. Y. Wu, Q. Li, L. Wang, J. A. Huang, and F. X. Liang, Adv. Funct. Mater. **24**, 2794–2800 (2014).
[40] G. Isić, M. Jakovljević, M. Filipović, D. Jovanović, B. Vasić, S. Lazović, N. Puač, Z. L. Petrović, R. Kostić, R. Gajić, J. Humlíček, M. Losurdo, G. Bruno, I. Bergmair, and K. Hingerl. J. Nanophoton. **5**, 051809 (2011).
[41] Y. Y. Liu, R. Miao, G. W. She, L. X. Mu, Y. Wang, and W. S. Shi, J. Phys. Chem. C. **115**, 21599–21603 (2011).
[42] T. Maeda, S. Takagi, T. Ohnishi, and M. Lippmaa Mater. Sci. Semicon. Proc. **9**, 706–710 (2006).
[43] S. S. Kim, S. Y. Choi, C. G. Park, and H. W. Jin, Thin Solid Films. **347**, 155–160 (1999).
[44] S. V. Zhukovsky, V. E. Babicheva, A. V. Uskov, I. E. Protsenko, and A. V. Lavrinenko, Plasmonics. **9**, 283–289 (2013).

© 2016 by WILEY-VCH Verlag GmbH & Co. KGaA, Weinheim

[45] X. C. Miao, S. Tongay, M. K. Petterson, K. Berke, A. G. Rinzler, B. R. Appleton, and A. F. Hebard, Nano Lett. **12**, 2745–2750 (2012).
[46] J. M. Liu, Photonic Devices, (Cambridge University Press, Cambridge, 2005).
[47] K. W. Liu, M. Sakurai, M. Y. Liao, and M. Aono, J. Phys. Chem. C **114**, 19835–19839 (2010).
[48] L. B. Luo, X. L. Huang, M. Z. Wang, C. Xie, C. Y. Wu, J. G. Hu, L. Wang, and J. A. Huang, Small. **10**, 2645–2652 (2014).
[49] Z. H. Zhang, L. B. Zhang, M. N. Hedhili, H. N. Zhang, and P. Wang, Nano Lett. **13**, 14–20 (2013).
[50] S. Linic, P. Christopher, and D. B. Ingram, Nature Mater. **10**, 911–921 (2011).
[51] L. H. Zeng, M. Z. Wang, H. Hu, B. Nie, Y. Q. Yu, C. Y. Wu, L. Wang, J. G. Hu, C. Xie, F. X. Liang, and L. B. Luo, ACS Appl. Mater. Interfaces **5**, 9362–9366 (2013).
[52] C. Y. Yan, N. Singh, H. Cai, C. L. Gan, and P. S. Lee, ACS Appl. Mater. Interfaces **2**, 1794–1797 (2010).

© 2016 by WILEY-VCH Verlag GmbH & Co. KGaA, Weinheim